The International Journal of Advanced Manufacturing Technology (2019) 100:2915–2927
https://doi.org/10.1007/s00170-018-2886-9

ORIGINAL ARTICLE

Selective laser melting of porosity graded lattice structures for bone implants

Dalia Mahmoud [1] · M. A. Elbestawi [1]

Received: 10 July 2018 / Accepted: 10 October 2018 / Published online: 22 October 2018

Abstract

Porosity-graded lattice structures are used in bone implants to mimic natural bone properties. Rather than having uniform pore size distribution, the size distribution is gradually changed in a certain direction to achieve specific mechanical and biological properties. Selective laser melting (SLM) has been used to print uniform metallic lattice structures with high accuracy. However, the accuracy of SLM in printing lattice structures with a wide range of pore sizes and volume fractions needs to be defined. The effect of SLM process scanning strategies on morphological properties of graded porosity metallic lattice structures is investigated in this study. Three different scanning strategies are proposed, and their effect on volume fraction, strut size, and surface integrity is investigated. Characterization of the printed parts reveals that the effect of different scanning strategies on the morphological quality is highly dependent on the design volume fraction for the chosen unit cell design. It was noted that using hatching strategies results in better dimensional accuracy and surface integrity in high-volume fraction lattice structures. While the use of total fill scanning strategy resulted in significantly distorted geometries in high-volume fractions. However, in lower-volume fractions, the dimensional accuracy as well as the surface integrity are comparable to that of hatching strategies. This work highlights the importance of understanding the limitations and capabilities of the SLM process in this application, and to enhance the printing quality of porosity-graded metallic lattice structures.

Keywords Selective laser melting · Porosity-graded lattice structures · Gyroids · Dimensional accuracy · Surface integrity

1 Introduction

Additive manufacturing (AM) technology is capable of printing customized biomedical implants, precisely tailored to the anatomy of each patient. Compared to other implant manufacturing methods, AM can print implants with lower costs, less material waste, and shorter times [1, 2]. Another important advantage beside customization is its ability to print implants from lattice structures instead of bulk/solid parts. The use of lattice structures in orthopedic implants accomplishes two important functional enhancements to the implants. The first is that lattice structures reduce the stiffness of the implant, therefore avoiding the stress shielding phenomena [3]. The second is that the presence of interconnected pore structure in the contact surface between the implant and the bone facilitate the bone tissue growth [4]. Selective laser melting (SLM) is an AM technology that is widely used for printing metallic parts, reaching an accuracy of 0.2 mm or less [5]. This has made it one of the most suitable techniques for printing lattice structures used for bone implants.

Porosity-graded lattice structures can be designed using computer-aided design (CAD) software or based on implicit equations [6]. Implicit equations are used to create triply periodic minimal surface (TPMS) unit cells [7], which are known for their biomorphic design, high surface area to volume ratio, interconnected pore channels, high permeability, and adequate mechanical integrity [8]. Furthermore, TPMS unit cells are considered self-supporting structures and therefore are well suited to be manufactured by SLM. Compared to CAD-based designs, the implicit-based unit cells can be manufactured with fewer defects [9]. These types of unit cells are also known for their ability to be designed in a continuous porosity gradation in contrast to the discontinuity between layers resulting from CAD unit cells.

✉ Dalia Mahmoud
mahmoudd@mcmaster.ca

✉ M. A. Elbestawi
elbestaw@mcmaster.ca

[1] Department of Mechanical Engineering, McMaster University, 1280 Main Street West, Hamilton, ON L8S 4L7, Canada

Lattice structures are formed from repetitive unit cells. The amount of porosity in these unit cells affects the mechanical and biological properties of lattice structures [10]. Large pore size (high porosity) allows more flow of nutrients and therefore enhances tissue growth [11]. However, this affects the mechanical properties of the lattice structure, and may become inadequate for bone implant applications [12]. To avoid this trade-off between mechanical and biological properties, porosity-graded lattice structures represent a good alternative. The mechanical properties of linear porosity-graded lattice structures show better mechanical properties than uniform ones [13, 14]. Onal et al. [15] tailored the porosity in the linear direction to obtain mirror-like structures with porosity increasing towards the center and vice versa. The authors suggested that the most suitable design would have high porosity on the outer volumes to enhance biological properties and prevent cell occlusions. Their results proved that small porosity in the inner volumes would enhance the mechanical integrity of the structures.

Although experimental results are promising, improper choice of SLM process parameters can lead to inconsistency and low repeatability. Investigating the effect of process parameters on the quality of printed lattice structures is required to optimize them. Few studies address the effects of SLM process parameters on the dimensional accuracy of lattice structures, and these studies primarily focused on uniform CAD-based lattice structures. A statistical approach to determine the manufacturability of Ti6Al4V CAD-based lattice structure was performed by Sing et al. [16, 17], where the laser power was found to be the most significant parameter influencing dimensional accuracy and mechanical properties. Ahmadi et al. [18] studied the effect of laser power and exposure time on the dimensional and mechanical properties of CAD-based lattice structures. It was found that for the intervals used in their study, increasing the laser power and exposure time increases the strut size and relative density of lattice structure. Therefore, the mechanical properties improve as well. The highest laser power used was 128 W, although higher laser powers can be used with Ti6Al4V.

The laser beam scan path can be varied in SLM process, as the laser path changes the thermal distribution and thermal history also changes. This leads to change in powder melting and solidification rates and thus affects the morphological and mechanical properties of printed parts [19]. The effect of scanning strategy on the quality of lattice structures is usually overlooked. Ghouse et al. [20] studied the influence of SLM scanning strategies and process parameters on stochastic lattice structures. Three scanning strategies were investigated: contouring, point, and pulsing strategies. The authors observed that those scanning strategies had no major effect on the strut thickness. It is assumed that changing the unit cell design (geometry) will change the effect of scanning strategies on the strut morphology.

Most of the afore-mentioned results targeted either CAD-based lattice structures or uniform graded ones. The lack of knowledge and understanding about TPMS lattice structure design makes it less understood than CAD-based lattice structures. Therefore, this study aims to investigate the manufacturability of porosity-graded TPMS lattice structures. First, the design space of one type of TPMS unit cells is investigated, relating the biological needs for bone implants and SLM capabilities with the unit cell's morphology. Then the effect of scanning strategy on the morphology of graded lattice structures is investigated. The density, dimensional accuracy, and surface integrity are examined, since they are the main contributing factors that affect lattice structures' mechanical and biological properties for bone implants.

2 Design of porosity-graded lattice structures

Gyroids are one type of TPMS that have been studied extensively over the past decade. Compared to other TPMS unit cells, gyroids are known for their comparatively good mechanical and biological properties [21, 22]. Gyroid surface can be defined by the parametric equation:

$$\mathrm{G} = \cos\left(\frac{2\pi}{L}\cdot x\right)\sin\left(\frac{2\pi}{L}\cdot y\right) + \cos\left(\frac{2\pi}{L}\cdot y\right)\sin\left(\frac{2\pi}{L}\cdot z\right) + \cos\left(\frac{2\pi}{L}\cdot z\right)\sin\left(\frac{2\pi}{L}\cdot x\right) - t = 0 \quad (1)$$

where L is the size of each unit cell as shown in Fig. 1 and t is the "level constant" that controls the volume fraction of each unit cell. Volume fraction is the ratio between the volume of material and volume of the unit cell (L^3). Like sine and cosine waves, the gyroid surface has a period that could be scaled to control the lattice size and number of pores. By changing the value of t, the volume fraction of each unit cell changes as well.

The mathematical equation provides insight into the morphology of gyroids which allows for better understanding of gyroid lattice structures. The relationship between the equation inputs, t and L, and the gyroid lattice outputs, volume fraction, strut size, and pore size, were investigated. A MATLAB® code was written to create gyroid lattice structures in STL (stereolithography) format. Then the file was imported to Netfabb®, for post-processing and measurements. Thirty single-unit cells were created at different values of t; the volume fraction relationship with t is plotted in Fig. 2a. As the value of t increases, the volume fraction increases as well. When $t = 0$, the gyroid surface divides the space into two equal domains; thus, the unit cell would have a volume fraction of 50%. For t values greater than 1.5, the unit cell turns into solid,

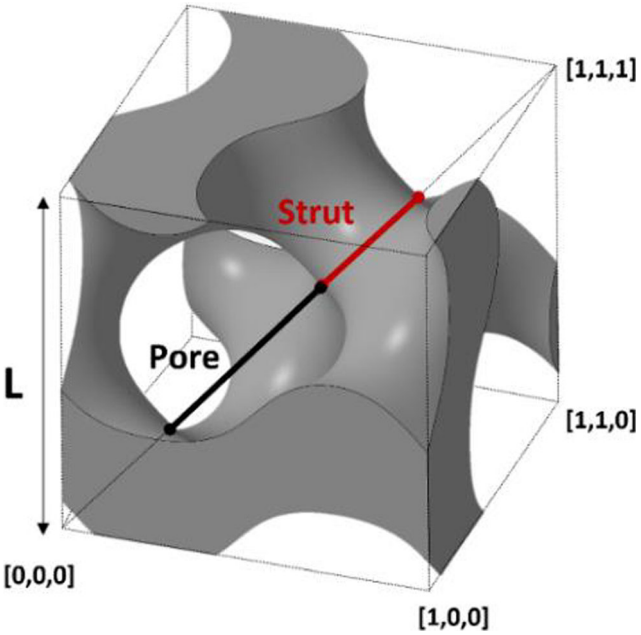

Fig. 1 Morphology of a single gyroid unit cell

while for values of t below − 1.5, the gyroid equation does not exist.

The strut and pore sizes are also measured using Netfabb®; the strut size of the gyroid would differ in each location. Therefore, all the measurements were taken at the intersection between a vector in the direction of [111] and the gyroid unit cell as explain by Walker et al. [28]. As illustrated by Fig. 2b, as the value of t increases, the volume fraction increases, the pore size increases, and the strut size decreases. As the equations for regression were obtained, the morphology (i.e., volume fraction, strut size, and pore size) can be determined using two input parameters, t and L. Volume fraction, pore size, and strut thickness play an important role to define the bone cell attachment to the bone implant. Therefore, the permissibility design space would vary from one unit cell to the other [23]. The minimum strut thickness to be manufactured using SLM can be defined by 0.2 mm [24]. The bone volume to total volume (volume fraction) of trabecular bone is in the range of 5 to 60% (95–40% porosity), while that of cortical is 85–95% (5–15% porosity). The morphological requirements for trabecular and cortical bone differ according to the region of the body [25]; for example, the average pore size for trabecular bone in a femoral head is in the range of 0.456–0.982 mm, while that of the vertebrae is around 0.922 mm. For bone growth requirement, porosity higher than 50% is essential, and pore size between 0.609 and 0.110 mm is needed [26, 27]

Figure 3 illustrates the permissible design space for gyroid unit cells. Pore and strut size distributions are plotted in dotted lines for different unit cell sizes. The biological requirements for successful implants are represented in the red lines, while the SLM capability is presented in black line. The shaded area represents the allowable design space for gyroid lattice structures for bone implant applications. The map acts as a guide to determine the gyroid's morphological outputs from the equation inputs (t, L). It facilitates the choice of the correct parameters to match the bone implants' requirements and capabilities of SLM.

3 Experimental work

3.1 Materials and methods

The porosity-graded gyroids (PGGs) printed in this study were obtained using the gyroid equations. By replacing the constant value of t to a linear function, the porosity gradation/change in volume fraction design is displayed

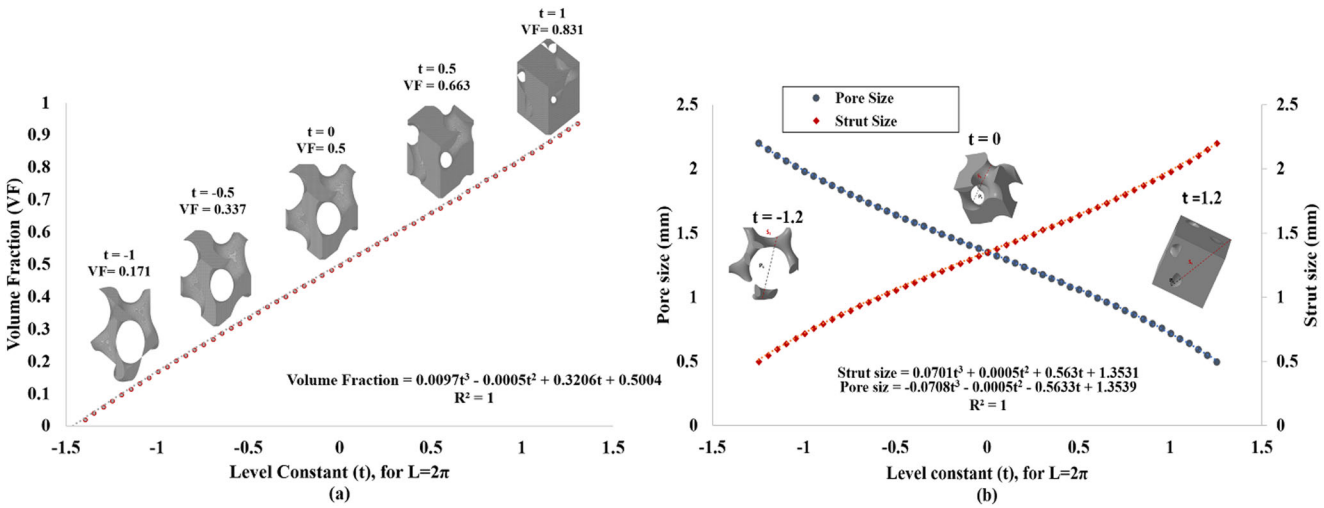

Fig. 2 **a** Volume fraction. **b** Strut and pore size as a function of level constant (t) for gyroid unit cell

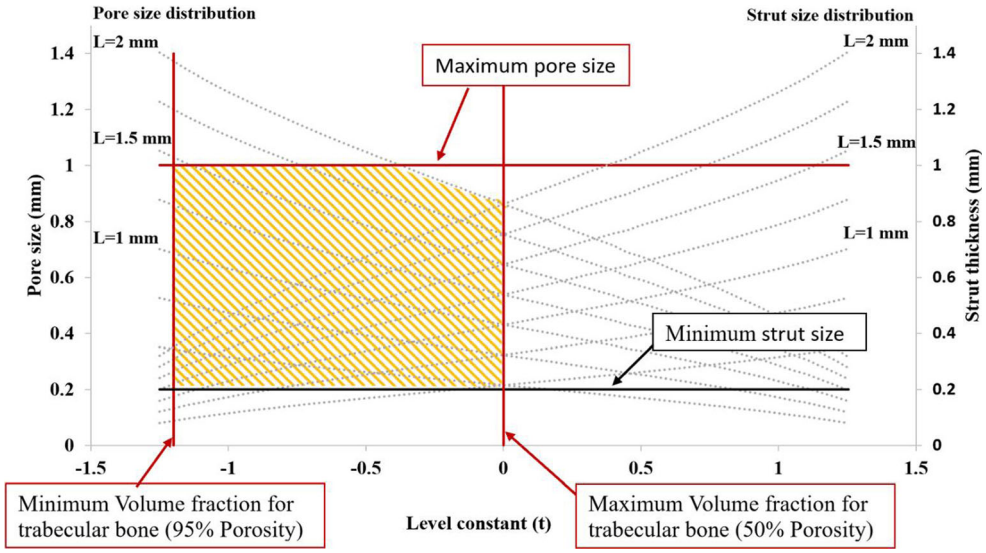

Fig. 3 Permissibility design space for gyroid unit cells

in Fig. 4. By setting the value of L to 1 mm and using boundary limits (− 0.5 to 9.5π), 10 × 10 × 10-mm cubes were created in a stereolithography "STL" format. A solid base layer of 5 mm was added to the part, to facilitate adhesion and removal from the build plate. One major advantage of that type of structure is that the change in the geometry is continuous. Therefore, no sudden interruptions between layers occur, ensuring a continuous change between layers.

A Renishaw AM400 machine (Renishaw Solution Center, Kitchener, ON, Canada) equipped with 400-W pulsed fiber laser was used to manufacture the PGGs. Titanium is one of the most common alloys to be used for bone implant applications [29]; for this study, Ti6Al4V ELI-0406 powder supplied by Renishaw was used. Three PGGs were printed using fixed process parameters, reported in Table 1. For each PGG, a different scanning strategy was used. As built, PGGs were ultrasonically cleaned in acetone and ethanol for 10 min each. Then compressed air was used to make sure no trapped powder was stuck inside the structures.

Table 1 SLM process parameters

Power	200 W
Exposure time	75 μm
Point distance	50 μm
Hatch distance	65 μm
Layer thickness	30 μm
Layer power at boarder	100 W
Contour offset distance	60 μm

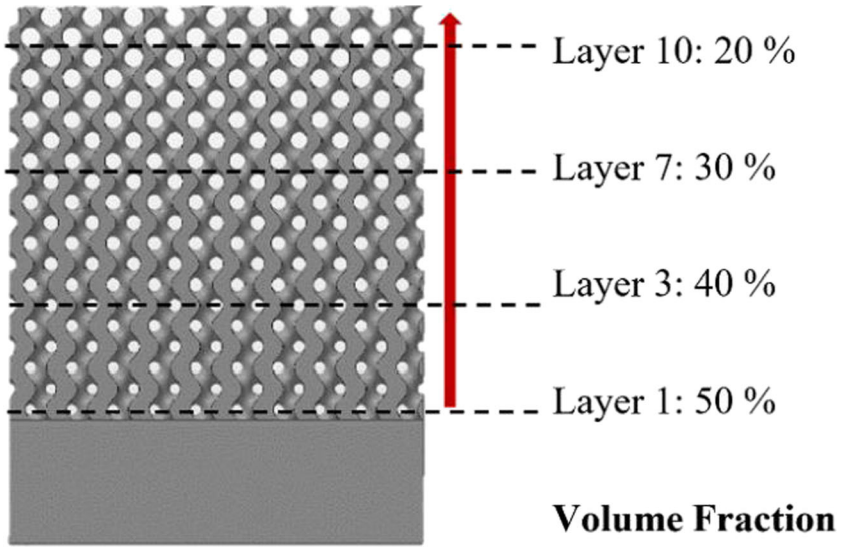

Fig. 4 Porosity-graded gyroids (PGGs)

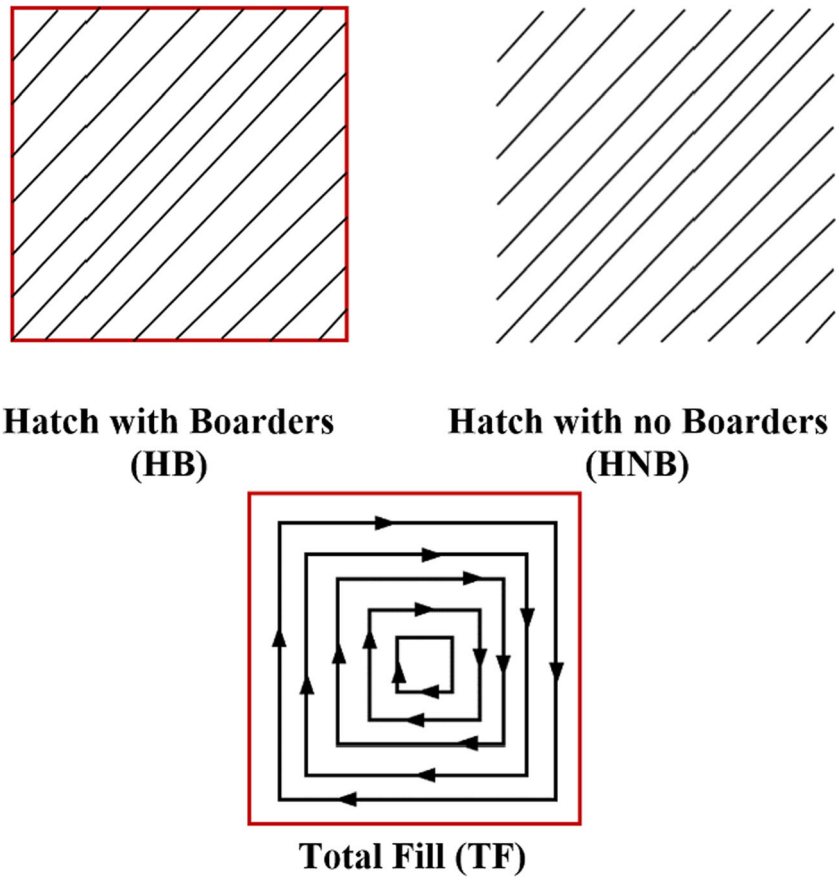

Fig. 5 SLM scanning strategies used for printing the PGGs

3.2 Scanning strategies

Three different scanning strategies were investigated: hatching with boarder (HB), hatching with no boarders (HNB), and total fill (TF). Figure 5 represents the schematic laser path for each of these strategies. The HNB scan strategy consists of scanning stripes oriented with 67° in the first layer. The second layer is rotated by 67° relative to the first one to reduce the residual stresses [30]. Residual stresses are caused when high thermal stresses are introduced to the part, while the part volume is not free to expand or contract [31]. In the HB strategy, the hatching is first scanned by the same strategy as HNB, and at the end one final contour is scanned around the hatches. In TF strategy, the layer is printed by making concentric contours of the geometry until the whole part is covered. In this strategy, the laser moves from inner contours to outer ones, and there is no rotation between two successive layers.

3.3 Volume fraction

Four different methods were used to obtain the density of the PGGs: dry weighting, Archimedes principle using water, Archimedes using acetone, and microcomputed tomography (μCT). Dry weighing simply weighs the part and divides it by its measured volume to obtain the calculated density. The volume fraction is calculated by dividing the calculated density on the theoretical density of the material used [16]. Archimedes principle was used to determine the density of the porosity graded lattice structures. The weight of each part was measured in the air and water using a digital scale (accuracy of ± 0.01 g); the process was repeated three times for reliability. The relative density was calculated by dividing the calculated density of the lattice structure by the relative density of Ti6Al4V alloy (4.42 g/cm^3). Next, acetone was used instead of water, and the whole process was repeated, replacing the density of water by that of acetone. A Bruker SkyScan1172 X-ray tomography scanner was used for quantitative analysis for the printed lattice structures at 100 kV using an Al/Cu filter. The total volume (10 × 10 × 10 mm^3) of the PGGs was scanned allowing a voxel resolution of 8.4 μm^3. Additionally, the volume fraction of each layer was evaluated using μCT, by obtaining the ratio between material and voids in each layer.

3.4 Dimensional accuracy

The reconstructed scans from the μCT were used to investigate the dimensional accuracy of the porosity-graded lattice

structures. Netfabb® was used for virtual measurements and post-processing of reconstructed scans. Reconstructed strut sizes in different layers were measured and compared to the design values. For consistent results, the strut size was measured in the direction of the [111] vector as described by Walker et al. [28]. Five randomly distributed readings were obtained in each layer of measurements to reduce errors. To obtain a better understanding of the strut variation, mesh comparisons were used to evaluate the overall variation between the design and the as built specimens.

3.5 Surface integrity

Due to the relatively small size of the struts and the large amount of partially melted powder, the roughness on some of the internal struts was inaccessible using optical methods. Surface roughness was characterized via stylus profilometry (Surftest Sj-410) on the outer flat surface of the PGGs. Side roughness was measured along the layer's direction; 5 mm of the surface was evaluated. A cutoff wavelength of 0.8 mm was used to determine the arithmetic average roughness "R_a"; this value ensured the proper distinguish between wave form roughness and the high-frequency ones. Five measurements were taken in each layer to reduce the errors and ensure reliability of results. A scanning electron microscope (SEM) was used to investigate the surface of the printed graded lattice structures.

4 Results and discussion

4.1 Visual evaluation

The primary focus of this work is to evaluate the effect of scanning strategies on the quality of porosity-graded lattice structures. Figure 6 represents the macroscopic evaluation of the as built PGGs. The PGG scanned using TF strategy failed in the first six layers; since the contours are concentric, contour overlapping may occur increasing the amount of laser input energy delivered to the powder [32]. The PGG scanned with HB strategy had better defined structure than the HNB

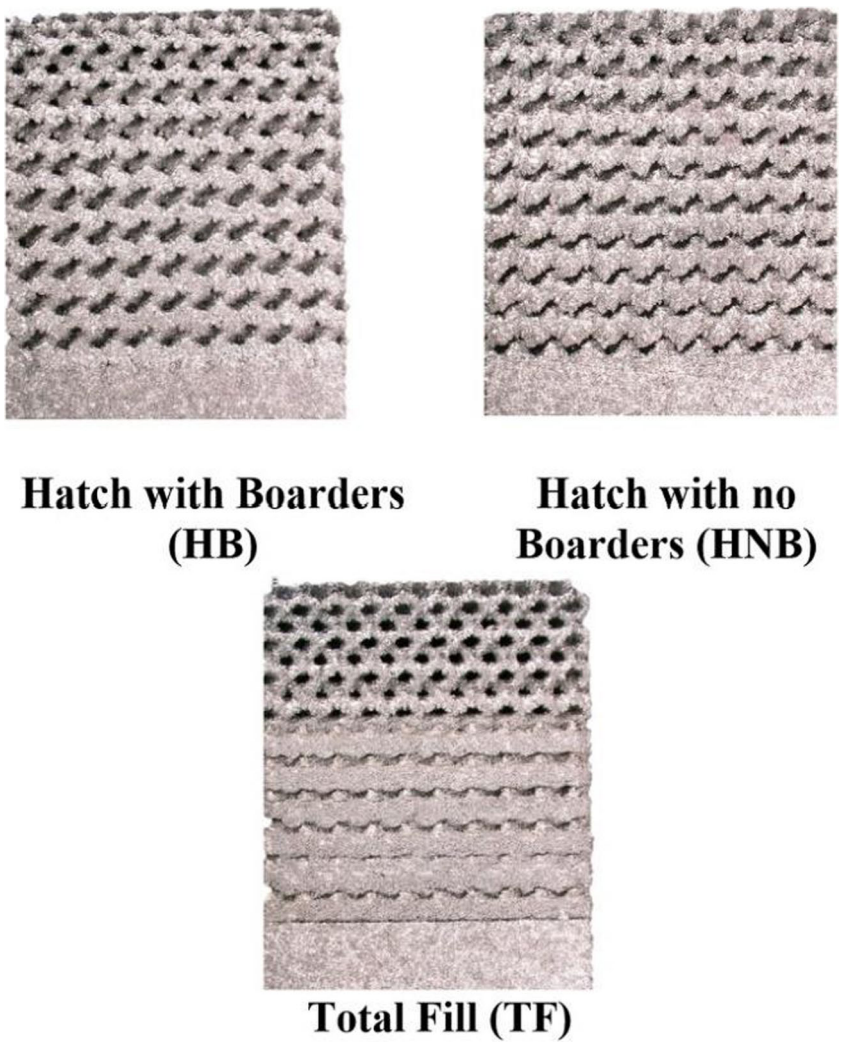

Fig. 6 Visual evaluation of PGGs

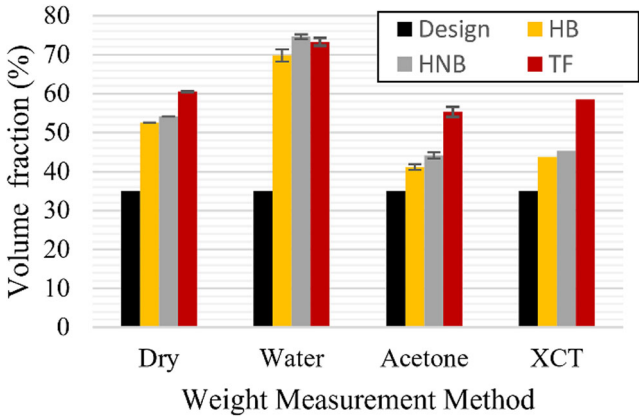

Fig. 7 Total volume fraction obtained from different measurement methods compared to corresponding design values

strategy; this is attributed to the final contour used for enhancing surface finish in this strategy [33]. Overall, the geometry of the pores appeared to be deviated from the design, and some pores appeared to be clogged. This may indicate that the process parameters chosen need some tuning to obtain more accurate geometry.

4.2 Volume fraction

The deviation in volume fraction using the four measurement methods for the three PGGs is illustrated by Fig. 7; all measurements were found to be greater than the designed volume fraction. Dry weighing overestimated the volume fraction due to the omission of the internal porosity. This method gives an indication of the general trend of the volume fractions. Using water as a suspension liquid in the Archimedes method gave an over estimation of the volume fraction as well. This can be attributed to the high surface roughness of the parts. Rough surfaces may lead to the formation of air bubbles and therefore results in inconsistent measurements [34]. Very low deviations between volume fraction measured using the Archimedes method using acetone and μCT were observed. These

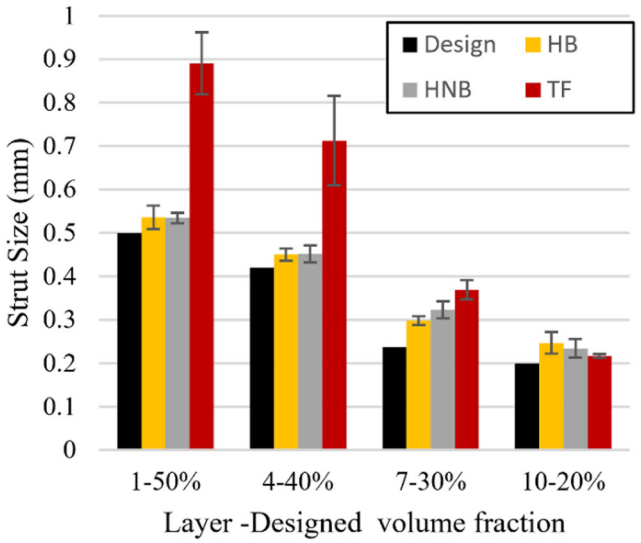

Fig. 9 Strut size obtained via μCT and compared to corresponding design values

methods were therefore considered more reliable than the other two methods. The variation between the two methods can be related to several factors such as the inability of acetone to penetrate the pores and the rough surface of the struts preventing the liquid to fully fill the voids. The presence of internal voids as well could not be detected using Archimedes methods. Some errors that might occur in μCT scanning include image thresholding, beam hardening, misalignment errors, and limited resolution [35].

Overall, the obtained volume fraction is higher than expected; this suggests that the PGGs are less porous than designed. This agrees with the findings of Ataee et al. [36] and Han et al. [37]. The volume fraction increase is attributed to the errors resulting in the small strut sizes, small pore sizes of the parts, and the partially melted powder to the struts. The PGG scanned by the HB strategy resulted in the least deviation, while the PGG scanned by TF strategy resulted in the largest deviation.

Fig. 8 Layer's volume fraction obtained via μCT and compared to corresponding design values

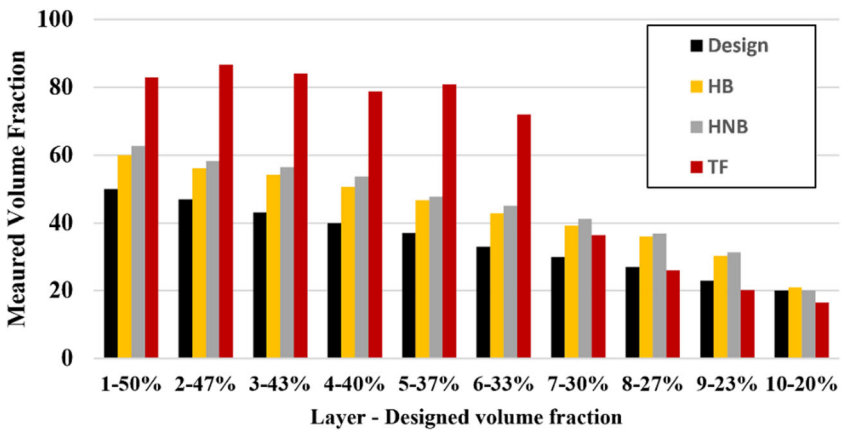

The deviation in volume fraction obtained from μCT reconstruction for each layer of the PGGs is plotted in Fig. 8. Visual evaluation of the first six layers in the PGG scanned using TF strategy gave the highest deviation. However, after the sixth layer (volume fraction = 30%), the deviation reduced significantly, reaching better results than the PGGs printed using HB and HNB strategies. The PGGs scanned using HB and NHB strategies show the same trend in volume fraction deviation. An average increase in volume fraction of 27 and 32% was evaluated for PGGs scanned by HB and HNB, respectively. The last layers in the three PGGs show less deviation in volume fraction. This can be attributed to the accumulative shrinkage in each layer of the PGGs, which was amplified in only the last layer. It might also be attributed to misalignment errors while CT scanning the PGGs. The variations can be better understood by evaluating dimensional accuracy of printed struts.

4.3 Dimensional accuracy

The strut sizes were measured in four different reconstructed layers (volume fractions = 50%, 40%, 30%, and 20%). The deviations in size between the design struts and the reconstructed struts are plotted in Fig. 9. The PGG scanned using TF strategy had significantly high size deviation in lower layers (high-volume fraction); these deviations are reduced significantly at upper layers (low-volume fraction). The PPGs scanned using HB and HNB strategies again show similar trends, with the HB strategy being more accurate. The measurements taken were randomly distributed from the same layer to make sure the results were consistent and reduce the errors resulting from misalignment while scanning. Average errors were in the order of 0.07 mm in the first layers (large struts), reaching a maximum of 0.25 mm in the last layers (small struts).

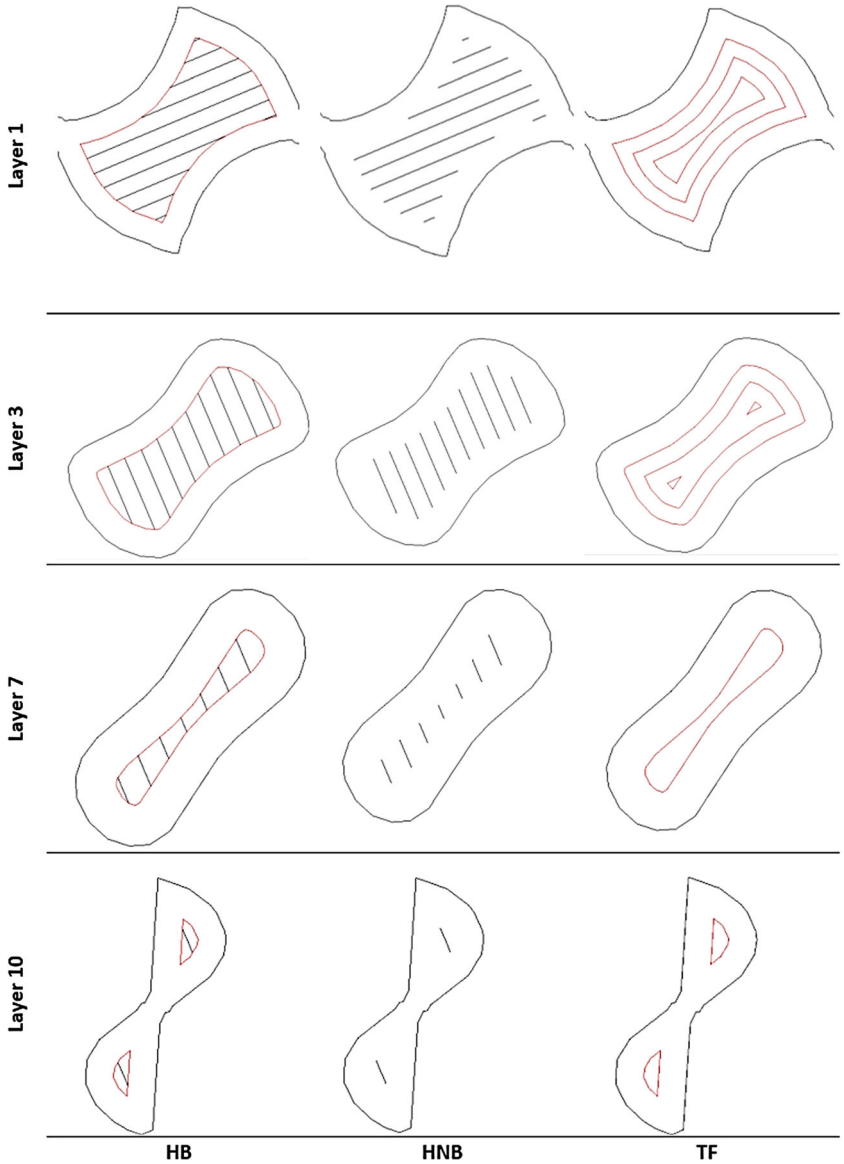

Fig. 10 Laser scanning strategies along different layers of PGGs

The TF strategy resulted in the highest errors in strut sizes in the first layers (high-volume fraction), when compared to HB and HNB strategies. By analyzing the scan path of the three scanning strategies as shown in Fig. 10, in the TF strategy, three contours are needed to cover the strut size geometry at the first layers. The process parameter settings determine the amount of energy delivered to the powder, therefore affects the meltpool size generated in each scan. The higher the laser energy input is, the larger the meltpool size is. The distance between hatch spacing and contours affects the meltpools to overlapping. Although overlapping is required to ensure good melt structure, too much overlapping can cause accumulation of energy [38]. It is assumed that the collapse of the first six layers is a result of large amount of energy generated from overlapping from concentric contours. In addition to the fact that no rotation occurs between successive layers in this strategy, which also accumulates the energy [32], this energy might be transferred to the layer below and re-melt it, thereby changing the strut dimensions, pore distribution, and volume fractions.

Large errors in small struts are attributed to the fact that the length of laser hatches is short and frequently repeated, and consequently, the small printed struts has no time to cool down. Kruth et al. [39] explained this phenomenon; the repetitive short scans increase the amount of laser energy input added to the small parts. Therefore, some accumulated energy may be conducted to the printed part sides leading to the adhesion of powder and resulting in an increase the measured volume fraction and strut size. This can be demonstrated by comparing the three laser scan paths used in this study, as illustrated by Fig. 10. Since repetitive scans are performed in HB and HNB strategies, more errors were found in these parts than the part scanned with the TF strategy. The TF strategy compared to HB and HNB needed almost one contour to fully build the strut.

It was noted that the struts on the corner of the last layers were highly deviated from other struts in the middle of this layer. Therefore, reconstruction of the last layer (volume fraction 20%) from the three parts were all compared to the design reference layer. The mesh comparison tool in Netfabb® was used to evaluate the difference between the reference (design)

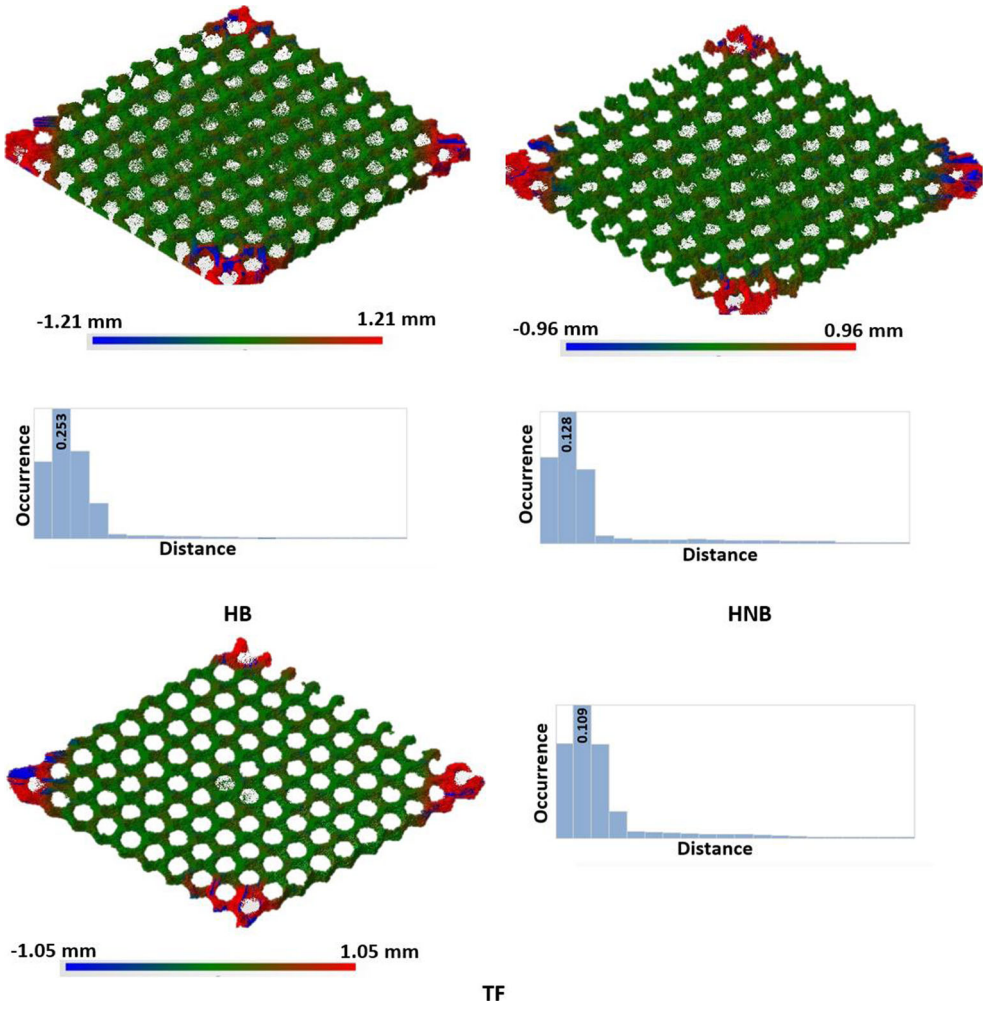

Fig. 11 Mesh comparison of μCT reconstruction and the CAD model for last layer of the three PGGs; red and blue represent the plus and minus errors. Histograms represent the occurrence of each value, dimensions in mm

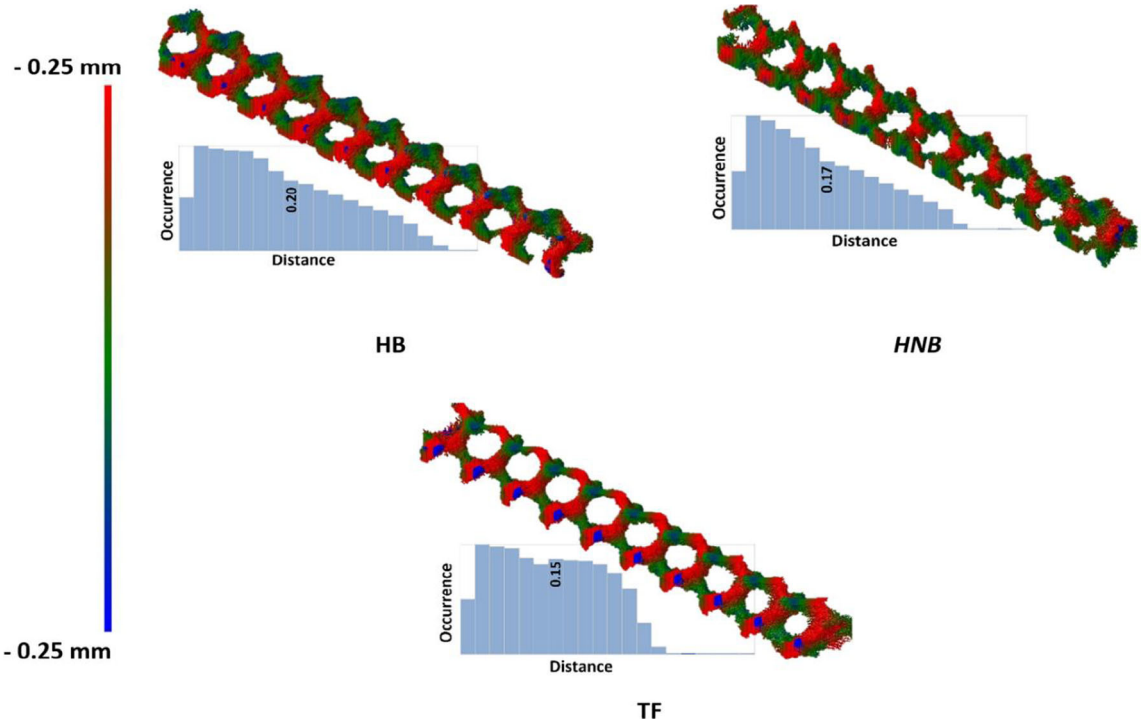

Fig. 12 Mesh comparison of one row from the last layer obtained via μCT and compared to the CAD model for the three PGGs; red and blue represent the plus and minus errors. Histograms represent the occurrence of each value, dimensions in mm

and the printed (reconstructed) layers. Figure 11 shows the mesh comparison for the last three layers of the printed PGGs. A notable deviation from the four corners was observed. Parts printed using HB strategy had the highest deviation (± 1.21 mm, with a high repeatability of 0.253 mm). This deviation can be attributed to the presence of residual stress after the parts are separated from the base plate.

To observe the deviation on a strut level, a single row of the last layer of each part was compared to the reference design. From mesh comparison, it was noted that errors in the PGG scanned by HB strategy were higher than the other strategies. All errors were found to be within ± 0.25 mm matching the results obtained from the vector [111] intersection with single reconstructed gyroid unit cells. Figure 12 displays the mesh comparison in each reconstructed layer. The benefit of using mesh comparison is to check the whole geometry, rather than one single position. For example, the PGGs scanned by HB and HNB strategies had large deviation in the diagonal struts, while the PGG scanned by TF strategy had some deviations in the struts but more deviations in the horizontal parts as well.

4.4 Surface integrity

The average surface roughness R_a values for different volume fractions are represented in Fig. 13. It is noted that at upper layers (lower volume fraction), the surface roughness

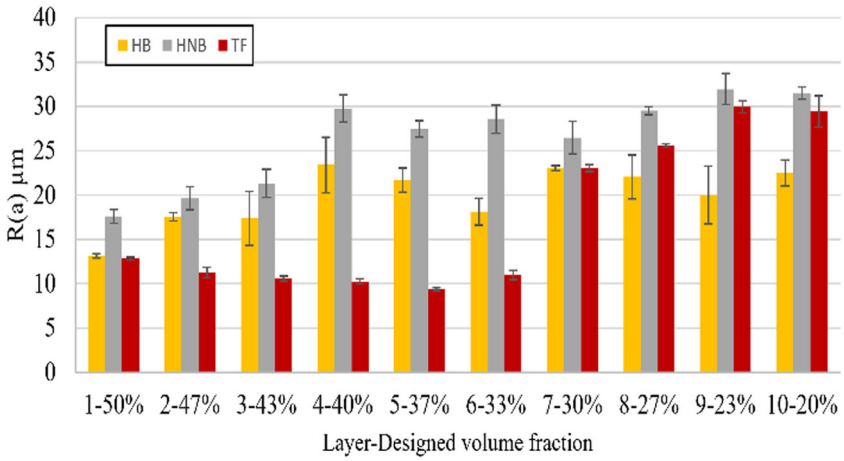

Fig. 13 Average surface roughness "R_a" values for each layer along the powder layer thickness

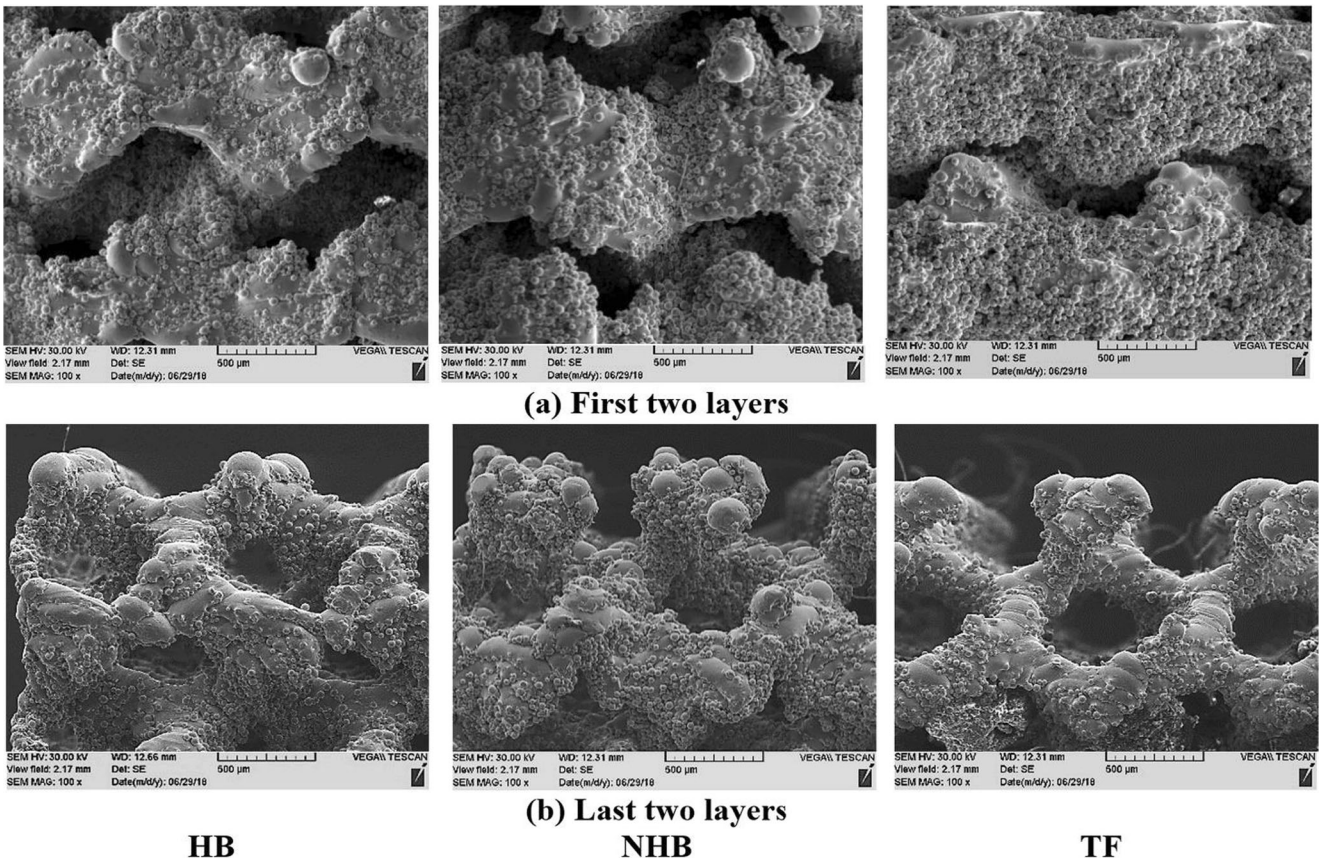

Fig. 14 SEM images of the **a** first two layers and **b** last two layers of the PGGs

increases. The main reason for this increase is attributed to the geometry of the gyroids. As the struts become thinner, the connection between two adjacent struts becomes thinner to the extent that it cannot be printed. Therefore, the upper layers are characterized by a sinewave that was evident in the scanned profile. The first six layers, parts printed using TF strategy, had a significantly lower surface roughness than the other two strategies. However, in the last four layers, it was noted that there was high variation in roughness. The PGGs scanned by HB strategy had the least R_a. However, according to Mumtaz et al. [40], R_a might not show strong correlation with the surface integrity. Therefore, to enhance the understanding of the surface integrity, SEM was used to investigate the parts.

The SEM images for the first three layers and the last three layers are represented in Fig. 14. The PGGs scanned by HB and HNB strategies were seen to have a high appearance of balling effects present in the first three layers. The balling phenomena can occur due to the instability of meltpool; small-sized droplets tend to splash out forming relatively large (micrometer-scaled) solidified spheres on the side of the printed parts [41]. Moreover, repetitive low-speed scans contribute to increasing the amount of energy in the meltpool, causing balling phenomena to appear in PGGs scanned by HB and HNB strategies [42]. The PGG scanned by the TF strategy had a significantly large amount of partially melted powder adhering to its surface. This can be attributed again to the scans overlap and the accumulated energy in these struts. The energy gets conducted to the surface; however, since it is not high enough to melt the surrounding powder, the powder gets partially melted to the sides.

In the upper layers (lower-volume fractions), the PGG scanned by HNB strategy have the highest amount of partially melted powder since no contour is made in this strategy. The surface of the PGG scanned by HB strategy has more partially melted powder and more non-uniform melted material compared to the part printed using TF strategy. This can be understood better by observing the laser scan paths presented by Fig. 10. In HB scanning strategy, the hatch intersects the outer boundary of the laser. If the laser meltpool generated from the hatches is bigger than the meltpool generated to create the boundary contour, this can lead to the appearance of balling phenomena and irregular surface. As for the HNB strategy, if the distance between two successive laser exposures is too far, it would result in an irregular surface as illustrated by Fig. 14b. The PGGs scanned using TF strategy need only one boarder contour to melt the whole area of the strut in the upper layers. Therefore, no overlapping between contours occurs and it is assumed that less accumulation of laser energy density occurs. Moreover, since there is no hatching in this strategy, the

undesirable effect of hatching and boarders intersecting is avoided. Hence, a more stable meltpool is evident and more melted tracks are detected.

5 Conclusion and future work

The scanning strategy in SLM was found to have a profound effect on the accuracy of printed lattice structures having porosity-graded gyroid design. This paper presents a guide for the design of porosity grading of TPMS lattice structures for bone implant applications. The morphologies of PGGs printed using SLM are investigated systematically, and the following conclusions are derived:

1- The measured volume fraction and strut sizes of PGGs are higher than the design values. These errors are attributed to the partially melted powder on the surface of the PGGs and inability of SLM to create small strut size with high accuracy.
2- Each layer of the PGGs is affected differently by the scanning strategies. In lower layers (high-volume fractions), the deviation in volume fraction and strut size is lower than that of the upper layers (low-volume fraction).
3- Meltpool size, hatch spacing, and contour spacing may be considered as key factors in enhancing the strut size accuracy.
4- The TF scanning strategy might not be suitable for high-volume fractions by the current process parameter settings. Proper control of the SLM process parameters would enhance both high- and low-volume fraction strut quality.

In this study, the process parameters recommended in the open literature for the SLM of bulk Ti6Al4V were used. These settings need to be adjusted for printing graded lattice structures. More research should target the "optimum" choice of laser energy density while printing those graded structures. Although the meltpool size and temperature were not measured in this study, it is suggested that they strongly affect the quality of the graded lattice structures. The precise monitoring of meltpool is considered extremely important to control the dimensional and surface integrity of printed graded lattice structures. The main objective should target reducing the amount of partially melted powder to the surfaces, enhance the dimensional accuracy, and surface integrity of the porosity-graded lattice structures.

Acknowledgments We acknowledge the support of the Natural Sciences and Engineering Research Council of Canada (NSERC; funding reference number 518494).

References

1. Cronskär M, Bäckström M, Rännar L-E (2013) Production of customized hip stem prostheses—a comparison between conventional machining and electron beam melting (EBM). Rapid Prototyp J 19: 365–372. https://doi.org/10.1108/RPJ-07-2011-0067
2. Harrysson OLA, Cansizoglu O, Marcellin-Little DJ, Cormier DR, West HA II (2008) Direct metal fabrication of titanium implants with tailored materials and mechanical properties using electron beam melting technology. Mater Sci Eng C 28:366–373. https://doi.org/10.1016/j.msec.2007.04.022
3. Huiskes R, Weinans H, van Rietbergen B (1992) The relationship between stress shielding and bone resorption around total hip stems and the effects of flexible materials. Clin Orthop Relat Res:124–134. https://doi.org/10.1097/00003086-199201000-00014
4. Van Der Stok J, Van Der Jagt OP, Amin Yavari S et al (2013) Selective laser melting-produced porous titanium scaffolds regenerate bone in critical size cortical bone defects. J Orthop Res 31: 792–799. https://doi.org/10.1002/jor.22293
5. Abele E, Stoffregen HA, Kniepkamp M, Lang S, Hampe M (2015) Selective laser melting for manufacturing of thin-walled porous elements. J Mater Process Technol 215:114–122. https://doi.org/10.1016/j.jmatprotec.2014.07.017
6. Helou M, Kara S (2017) Design, analysis and manufacturing of lattice structures: an overview. Int J Comput Integr Manuf 31: 243–261. https://doi.org/10.1080/0951192X.2017.1407456
7. Rajagopalan S, Robb RA (2006) Schwarz meets Schwann: design and fabrication of biomorphic and durataxic tissue engineering scaffolds. Med Image Anal 10:693–712. https://doi.org/10.1016/j.media.2006.06.001
8. Almeida HA, Bártolo PJ (2014) Design of tissue engineering scaffolds based on hyperbolic surfaces: structural numerical evaluation. Med Eng Phys 36:1033–1040. https://doi.org/10.1016/j.medengphy.2014.05.006
9. Yan C, Hao L, Hussein A, Young P (2015) Ti–6Al–4V triply periodic minimal surface structures for bone implants fabricated via selective laser melting. J Mech Behav Biomed Mater 51:61–73. https://doi.org/10.1016/j.jmbbm.2015.06.024
10. Kumar A, Nune KC, Murr LE, Misra RDK (2016) Biocompatibility and mechanical behaviour of three-dimensional scaffolds for biomedical devices: process–structure–property paradigm. Int Mater Rev 61:20–45. https://doi.org/10.1080/09506608.2015.1128310
11. Taniguchi N, Fujibayashi S, Takemoto M, Sasaki K, Otsuki B, Nakamura T, Matsushita T, Kokubo T, Matsuda S (2016) Effect of pore size on bone ingrowth into porous titanium implants fabricated by additive manufacturing: an in vivo experiment. Mater Sci Eng C 59:690–701. https://doi.org/10.1016/j.msec.2015.10.069
12. Ahmadi SM, Yavari SA, Wauthle R, Pouran B, Schrooten J, Weinans H, Zadpoor A (2015) Additively manufactured open-cell porous biomaterials made from six different space-filling unit cells: the mechanical and morphological properties. Materials (Basel) 8: 1871–1896. https://doi.org/10.3390/ma8041871
13. Zhang S, Li C, Hou W, Zhao S, Li S (2016) Longitudinal compression behavior of functionally graded Ti–6Al–4V meshes. J Mater Sci Technol 32:1098–1104. https://doi.org/10.1016/J.JMST.2016.02.008
14. Al-Saedi DSJ, Masood SH, Faizan-Ur-Rab M et al (2018) Mechanical properties and energy absorption capability of functionally graded F2BCC lattice fabricated by SLM. Mater Des 144:32–44. https://doi.org/10.1016/j.matdes.2018.01.059

15. Onal E, Frith JE, Jurg M, Wu X, Molotnikov A (2018) Mechanical properties and in vitro behavior of additively manufactured and functionally graded Ti6Al4V porous scaffolds. Metals (Basel) 8. https://doi.org/10.3390/met8040200
16. Sing SL, Wiria FE, Yeong WY (2018) Selective laser melting of lattice structures: a statistical approach to manufacturability and mechanical behavior. Robot Comput Integr Manuf 49:170–180. https://doi.org/10.1016/j.rcim.2017.06.006
17. Sing SL, Yeong WY, Wiria FE, Tay BY (2016) Characterization of titanium lattice structures fabricated by selective laser melting using an adapted compressive test method. Exp Mech 56:735–748. https://doi.org/10.1007/s11340-015-0117-y
18. Ahmadi SM, Hedayati R, Ashok Kumar Jain RK, Li Y, Leeflang S, Zadpoor AA (2017) Effects of laser processing parameters on the mechanical properties, topology, and microstructure of additively manufactured porous metallic biomaterials: a vector-based approach. Mater Des 134:234–243. https://doi.org/10.1016/j.matdes.2017.08.046
19. Dai D, Gu D, Zhang H, Xiong J, Ma C, Hong C, Poprawe R (2018) Influence of scan strategy and molten pool configuration on microstructures and tensile properties of selective laser melting additive manufactured aluminum based parts. Opt Laser Technol 99:91–100. https://doi.org/10.1016/J.OPTLASTEC.2017.08.015
20. Ghouse S, Babu S, Van Arkel RJ et al (2017) The influence of laser parameters and scanning strategies on the mechanical properties of a stochastic porous material. Mater Des 131:498–508. https://doi.org/10.1016/j.matdes.2017.06.041
21. Kapfer SC, Hyde ST, Mecke K, Arns CH, Schröder-Turk GE (2011) Minimal surface scaffold designs for tissue engineering. Biomaterials 32:6875–6882. https://doi.org/10.1016/j.biomaterials.2011.06.012
22. Melchels FPW, Bertoldi K, Gabbrielli R, Velders AH, Feijen J, Grijpma DW (2010) Mathematically defined tissue engineering scaffold architectures prepared by stereolithography. Biomaterials 31:6909–6916. https://doi.org/10.1016/j.biomaterials.2010.05.068
23. Melancon D, Bagheri ZS, Johnston RB, Liu L, Tanzer M, Pasini D (2017) Mechanical characterization of structurally porous biomaterials built via additive manufacturing: experiments, predictive models, and design maps for load-bearing bone replacement implants. Acta Biomater 63:350–368. https://doi.org/10.1016/j.actbio.2017.09.013
24. Arabnejad S, Burnett Johnston R, Pura JA, Singh B, Tanzer M, Pasini D (2016) High-strength porous biomaterials for bone replacement: a strategy to assess the interplay between cell morphology, mechanical properties, bone ingrowth and manufacturing constraints. Acta Biomater 30:345–356. https://doi.org/10.1016/j.actbio.2015.10.048
25. Bobbert FSL, Lietaert K, Eftekhari AA, Pouran B, Ahmadi SM, Weinans H, Zadpoor AA (2017) Additively manufactured metallic porous biomaterials based on minimal surfaces: a unique combination of topological, mechanical, and mass transport properties. Acta Biomater 53:572–584. https://doi.org/10.1016/j.actbio.2017.02.024
26. Heinl P, Müller L, Körner C, Singer RF, Müller FA (2008) Cellular Ti-6Al-4V structures with interconnected macro porosity for bone implants fabricated by selective electron beam melting. Acta Biomater 4:1536–1544. https://doi.org/10.1016/j.actbio.2008.03.013
27. Yang J, Cai H, Lv J, Zhang K, Leng H, Sun C, Wang Z, Liu Z (2014) In vivo study of a self-stabilizing artificial vertebral body fabricated by Electron beam melting. Spine (Phila Pa 1976) 39: E486–E492. https://doi.org/10.1097/BRS.0000000000000211
28. Walker JM, Bodamer E, Kleinfehn A, Luo Y, Becker M, Dean D (2017) Design and mechanical characterization of solid and highly porous 3D printed poly(propylene fumarate) scaffolds. Prog Addit Manuf 2:99–108. https://doi.org/10.1007/s40964-017-0021-3
29. Rack HJ, Qazi JI (2006) Titanium alloys for biomedical applications. Mater Sci Eng C 26:1269–1277. https://doi.org/10.1016/j.msec.2005.08.032
30. Mercelis P, Kruth J, Kruth J-P (2006) Residual stresses in selective laser sintering and selective laser melting residual stresses in selective laser sintering and selective laser melting. Rapid Prototyp 12: 254–265
31. Kruth J-P, Deckers J, Yasa E, Wauthlé R Assessing and comparing influencing factors of residual stresses in selective laser melting using a novel analysis method. https://doi.org/10.1177/0954405412437085
32. Kudzal A, McWilliams B, Hofmeister C, Kellogg F, Yu J, Taggart-Scarff J, Liang J (2017) Effect of scan pattern on the microstructure and mechanical properties of powder bed fusion additive manufactured 17-4 stainless steel. Mater Des 133:205–215. https://doi.org/10.1016/J.MATDES.2017.07.047
33. Schwanekamp T, Bräuer M, Reuber M (2017) Geometrical and topological potentialities and restrictions in selective laser sintering of customized carbide precision tools 49:
34. Ter HG, Becker T (2018) Selective laser melting produced Ti-6Al-4V: post-process heat treatments to achieve superior tensile properties. Materials (Basel) 11:146. https://doi.org/10.3390/ma11010146
35. Ho ST, Hutmacher DW (2006) A comparison of micro CT with other techniques used in the characterization of scaffolds. Biomaterials 27:1362–1376. https://doi.org/10.1016/J.BIOMATERIALS.2005.08.035
36. Ataee A, Li Y, Fraser D, Song G, Wen C (2018) Anisotropic Ti-6Al-4V gyroid scaffolds manufactured by electron beam melting (EBM) for bone implant applications. Mater Des 137:345–354. https://doi.org/10.1016/j.matdes.2017.10.040
37. Han C, Li Y, Wang Q, Wen S, Wei Q, Yan C, Hao L, Liu J, Shi Y (2018) Continuous functionally graded porous titanium scaffolds manufactured by selective laser melting for bone implants. J Mech Behav Biomed Mater 80:119–127. https://doi.org/10.1016/j.jmbbm.2018.01.013
38. Su X, Yang Y (2012) Research on track overlapping during selective laser melting of powders. J Mater Process Technol 212:2074–2079. https://doi.org/10.1016/J.JMATPROTEC.2012.05.012
39. Kruth JP, Froyen L, Van Vaerenbergh J et al (2004) Selective laser melting of iron-based powder. J Mater Process Technol 149:616–622. https://doi.org/10.1016/J.JMATPROTEC.2003.11.051
40. Mumtaz K, Hopkinson N (2009) Top surface and side roughness of Inconel 625 parts processed using selective laser melting. Rapid Prototyp J 15
41. Gu D, Shen Y (2009) Balling phenomena in direct laser sintering of stainless steel powder: metallurgical mechanisms and control methods. Mater Des 30:2903–2910. https://doi.org/10.1016/J.MATDES.2009.01.013
42. Mumtaz KA, Hopkinson N (2010) Selective laser melting of thin wall parts using pulse shaping. J Mater Process Technol 210:279–287. https://doi.org/10.1016/J.JMATPROTEC.2009.09.011